Oriented growth of layered-MnO$_2$ nanosheets over α-MnO$_2$ nanotubes for enhanced room-temperature HCHO oxidation

Jing Zhou, Lifan Qin, Wei Xiao*, Chen Zeng, Ni Li, Teng Lv, Hua Zhu*

School of Resource and Environmental Sciences, Hubei International Scientific and Technological Cooperation Base of Sustainable Resource and Energy, Wuhan University, Wuhan 430072, PR China

ARTICLE INFO

ABSTRACT

Construction of heterostructures with well-defined size, dimension, surface and interface is an effective approach to develop enhanced and unprecedented functionality. Herein, oriented growth of layered-MnO$_2$ nanosheets (L-MnO$_2$) over α-MnO$_2$ nanotubes backbones is demonstrated. The epitaxial relationship in the resulting α-MnO$_2$@L-MnO$_2$ heteroepitaxy is rationalized as (110)(α-MnO$_2$)||(001)(layered-MnO$_2$). With loading of 1 wt% Pt nanoparticles over the MnO$_2$ samples, the resulting Pt/MnO$_2$ samples show catalytic activity toward room-temperature HCHO oxidation via "$HCHO + O_2 = CO_2 + H_2O$". Upon 1 h treatment, 92.1% HCHO becomes mineralized over the Pt/α-MnO$_2$@L-MnO$_2$, higher than that of 81.3% and 75.9% for the Pt/α-MnO$_2$ and Pt/L-MnO$_2$. The oxidation of HCHO was well fitted with the second-order kinetic model, with the rate constant of the Pt/α-MnO$_2$@L-MnO$_2$ exceeding that of the Pt/α-MnO$_2$ and the Pt/L-MnO$_2$ by 2.27 and 5.92 times. Density-Functional-Theory (DFT) simulations show that α-MnO$_2$ {100} surface facilitates adsorption/activation of O$_2$, and layered-MnO$_2$ {001} surface is beneficial to desorption of resultant H$_2$O. The α-MnO$_2$@L-MnO$_2$ heteroepitaxy simultaneously integrates exposed facets of α-MnO$_2$ {100} surface and layered-MnO$_2$ {001} surface, in which the synergetic effect of the two surfaces leads to significantly enhanced room-temperature HCHO oxidation activity. The present study provides a rational design of manganese oxide-based catalysts for advanced environmental and energy applications.

© 2017 Elsevier B.V. All rights reserved.

1. Introduction

Indoor air quality is of prime importance since we spend three quarters time indoor. Volatile organic compounds (VOCs) are typical indoor air pollutants, which are mainly from building/decorative materials and unregulated indoor smoking. Formaldehyde (HCHO) is one of the most common VOC pollutants, causing profound impacts on human health. Therefore, strict environmental regulations are imposed to control indoor-air concentrations of gaseous HCHO [1]. In response, an assortment of technologies such as adsorption [2–4], plasma treatment [5,6], biological degradation [7], thermal catalytic oxidation [8–28] and photo-catalytic oxidation [29–31] are developed [1]. Amongst the aforenamed strategies, **room-temperature catalytic oxidation** is regarded as an affordable, convenient and complete disposal of

HCHO. The overall reaction of this method is represented as Reaction (1).

$$HCHO + O_2 = CO_2 + H_2O \tag{1}$$

The key-enabling factor of room-temperature HCHO oxidation is to develop high-efficiency catalysts to sustain Reaction (1). Besides fast and reversible redox capability, favorable adsorption of reactants and desorption of resultants are essential for an ideal catalyst. Incorporation of surface hydroxyl over oxide adsorbents was verified as an effective approach for enhanced HCHO adsorption, in which surface OH$^-$ could trigger Cannizzaro disproportionation of surface absorbed formaldehyde [2] and provide active H atoms [3] for additional HCHO adsorption. Enhanced oxidation of HCHO was reported by addition of alkali-metal ions to Pt/TiO$_2$ [17], due to activated H$_2$O reactivity and catalyzed reaction between surface hydroxyl and formate species.

Heterostructures are capable of providing enhanced physicochemical properties as a result of synergetic combinations of constituent building blocks as well as heterojunctions with unusual functionality. Heterostructures therefore offer enormous opportunities on tailoring functionality by a proper combination of

* Corresponding authors.
E-mail addresses: gabrielxiao@whu.edu.cn (W. Xiao), zhuhua333@126.com (H. Zhu).

components. Construction and utilization of heterostructures have become a research hotspot due to their extraordinary properties and significant application potential [32–42]. Heterostructures such as MnO_x-CeO_2,[8,15] TiO_2-Al_2O_3 [43,44], Fe_2O_3–MnO_2 [45], CuO–MnO_2 [45] and ZrO_2-poly(ethylene terephthalate) [46] were reported for enhanced room-temperature HCHO oxidation, with trace loading of precious co-catalysts.

Precise modulations of spatial, size and heterointerface in heterostructures are a determining aspect for triggering enhanced functionality and deep understanding the structure-activity correlations. In photocatalysis, proper heterojunctions render effective separation of photo-induced electron-hole pairs [32–38]. In contrast, heterointerfaces containing impurities and/or buffer layers tends to deteriorate spatial separation of photo-induced electron-hole pairs by functioning as recombination centers [34]. Therefore, spatial and size control of each component and interfaces in heterostructures is of importance, which, however, remains a challenge.

Oriented growth is regarded as one of the best protocols to attain a well-defined heterostructure with clean interface [39], in which epitaxial growth of branches over stems offers well-defined growth orientation and minimized cross-contamination in interface. The corresponding heteroepitaxy therefore possesses well-defined spatial and size configurations as well as clean heterointerface. The underlying scientific grounds for controllable construction of the heteroepitaxy lie in establishing facet couples between branches and backbones. For instance, d-spacing of (004) plane of hausmannite-Mn_3O_4 (0.23670 nm) is roughly one third of d-spacing of (001) plane of layered-MnO_2 (0.70498 nm). Such a facet couple based on crystallographic match endows oriented growth of layered MnO_2 nanosheets over hausmannite-Mn_3O_4 octahedra with exposed {101} facets, in which a clean interface is present [39].

Such a facet coupling is quite common between components with the same dimensions. The corresponding axial and lateral epitaxial growth of one-dimensional (1D) [36,41,42] and two-dimensional (2D) [33,35] heteroepitaxy are proven to be successful and generic. In the above scenario, similar crystallographic configurations in the interface of the 1D/1D and 2D/2D heteroepitaxy facilitate the oriented growth. However, construction of 1D/2D heteroepitaxy remains a challenge, mainly due to the broken crystallographic similarity in heterointerface.

In this contribution, we propose a straightforward strategy to controllable preparation of 1D/2D heteroepitaxy by employing the "rolling-cum-phase transformation" effect. Generally, 2D nanostructures with high surface energy tends to curl and roll into 1D nanostructures, governed by the "rolling-cum-phase transformation" mechanism [47]. The corresponding 1D and 2D nanostructures have inherent facet coupling, which forms the scientific basis for oriented growth between the 1D and 2D counterparts. Such a protocol for preparation of 1D/2D heteroepitaxy (notated as α-MnO_2@L-MnO_2) is herein demonstrated as oriented growth layered MnO_2 nanosheets (denoted as L-MnO_2) over α-MnO_2 nanotubes. The epitaxial relationship between layered MnO_2 branches and α-MnO_2 backbones is rationalized. After incorporation of trace Pt nanoparticles (i.e. 1 wt%), the Pt/α-MnO_2@L-MnO_2 shows enhanced catalytic capability than that of Pt/α-MnO_2 and Pt/L-MnO_2 and excellent cycle stability toward room-temperature oxidation of HCHO due to the synergetic combination between each component. Density-Functional-Theory (DFT) simulations indicate that α-MnO_2 has strong adsorption/activation of O_2 and layered-MnO_2 facilitates desorption of H_2O. The present study provides scientific insights on rational designs of affordable and efficient catalysts for thermal catalytic oxidation.

2. Experimental section

The experimental details are provided in the Supporting Information (SI).

The individual α-MnO_2 and L-MnO_2 were prepared by a reported hydrothermal preparation with minor modifications [48,49]. The hybrid MnO_2 (α-MnO_2@L-MnO_2) was constructed by a facile seed-epitaxial route employing the synthesized α-MnO_2 as seeds [39]. To prepare Pt/MnO_2 samples, 300 mg MnO_2 powder (α-MnO_2, L-MnO_2 and α-MnO_2@L-MnO_2) was dispersed in 10 mL deionized (DI) water, and then mixed with 0.8 mL of H_2PtCl_6 solution (0.0193 M) under magnetic stirring. Afterward, 5 mL of the mixed aqueous solutions of $NaBH_4$ solution (0.572 M), NaOH solution (0.25 M) and sodium citrate solution (1 mM) was quickly added into the suspension under vigorous stirring at 60 °C for 1 h. Finally, the sample was washed and centrifuged with DI water, and dried at 60 °C for 12 h. The content of Pt in the Pt/MnO_2 samples is controlled to be 1 wt%. The samples were represented as Pt/α-MnO_2, Pt/L-MnO_2 and Pt/α-MnO_2@L-MnO_2.

Room-temperature removal of HCHO was carried out in a 6 L organic glass box covered by a layer of aluminum foil on its inner wall [14]. 100 mg catalyst powder was dispersed on the bottom of a glass Petri dish with a diameter of 14 cm. After placing the sample-containing dish at the bottom of the reactor with a glass slide cover, 25 μL of formaldehyde solution (CAS No. 50-00-0, 37 wt% in water, contains 10–15% methanol as stabilizer to prevent polymerization) was injected into the reactor with a 5 W fan at the bottom of reactor. The HCHO solution completely volatilized and the concentration of HCHO quickly became stabilized at 300 ± 10 ppm. The adsorption and catalytic oxidation tests were carried out at room temperature (23 ± 2 °C). The relative humidity inside the organic glass box remained unchanged. The relative humidity in the laboratory was near 75%. In the present static experimental setup, it is of challenge to precisely tailor the relative humidity in the reaction box. The influence of relative humidity was previously investigated over Mn—Co—O [26] and Pt/TiO_2 [27]. The above references suggest that water enhances HCHO oxidation. Therefore, higher relative humidity is beneficial to HCHO oxidation, in which water acts as a promoter to generate more surface hydroxyls and enhance removal of intermediates.

The initial concentration of HCHO was controlled at ~300 ppm, which remained constant until the removal of the glass slide cover from the Petri dish to trigger the adsorption or catalytic oxidation reaction of HCHO. The concentrations of CO_2 and HCHO were online recorded using a Photoacoustic IR Multigas Monitor (INNOVA air Tech Instruments Model 1412) to evaluate the adsorption and catalytic performance. In the recycling experiments, no generations were carried out.

Density-Functional-Theory (DFT) calculations were used to investigate surface chemistry of the MnO_2 samples (α-MnO_2 {100} surface and layered-MnO_2 {001} surface). All DFT calculations were performed by CASTEP package on the basis of the plane-wave-pseudo-potential approach. The Perdew-Burke-Ernzerhof (PBE) of the generalized gradient approximation (GGA) was used as the exchange-correlation function. The interaction between valence electrons and ionic core was described by the ultrasoft pseudo-potential. The higher cutoff energy and the wider Monkhorst-Pack k-point mesh were tested. The obtained results suggested that the variations were smaller than 0.005 Å in displacement and 0.005 eV in energy, indicating the high accuracy of present calculations. The calculation smearing on adsorption energy is lower than 0.015 eV, which can satisfy the requirement of theoretical calculation. More information is provided in the SI.

3. Results and discussion

3.1. Construction of α-MnO$_2$@L-MnO$_2$ heteroepitaxy

By simply varying the temperatures, α-MnO$_2$ and L-MnO$_2$ were controllably prepared by hydrothermal treatment of aqueous KMnO$_4$ and HCl [48,49]. Upon hydrothermal treatment for 12 h at 140 °C and 95 °C, α-MnO$_2$ and L-MnO$_2$ are obtained, respectively. As evidenced by the corresponding XRD patterns shown in Fig. 1 (the upper panel), the two patterns are well indexed to α-MnO$_2$ (JCPDS No. 44-0141, tetragonal, *I4/m*, $a = b = 9.78$ Å, $c = 2.86$ Å) and layered-MnO$_2$ (JCPDS No. 80-1098, monoclinic, *C2/m*, $a = 5.15$ Å, $b = 2.84$ Å, $c = 7.17$ Å). The above XRD clearly show that the (110) diffraction peak of α-MnO$_2$ and (001) peak of layered-MnO$_2$ diffraction peak locate at very similar positions. As schematically illustrated in Fig. 1 (the below panel), the *d*-spacing of (110) plane of α-MnO$_2$ is 0.6919 nm, while the *d*-spacing of (001) plane of layered-MnO$_2$ is 0.70498 nm. The two values are comparable, forming the scientific grounds of the oriented growth between layered-MnO$_2$ and α-MnO$_2$.

Fig. 2 shows the scanning electron microscopy (SEM) and transmission electron microscopy (TEM) images of the prepared α-MnO$_2$ and L-MnO$_2$. As shown in Fig. 2a and c, the prepared α-MnO$_2$ is of nanotubes with well-defined tetragonal cross sections and smooth surface. It was documented that the α-MnO$_2$ nanotubes grows along the [001] direction and are enclosed with exposed (200) facets [49]. Fig. 2b clearly shows the formation of L-MnO$_2$ nanosheets. The exposed facets of the L-MnO$_2$ nanosheets are (001) [49]. In line with an epitaxial relationship of (110)(α-MnO$_2$)||(001)(L-MnO$_2$), the direct heteroepitaxial growth of L-MnO$_2$ nanosheets over α-MnO$_2$ nanotubes is proposed and schematically illustrated in Fig. 3a. In such a heteroepitaxy, the growth direction of branched L-MnO$_2$ nanosheets is perpendicular to the longitudinal axis of the nanotube stem (i.e. [001] direction).

The as-obtained α-MnO$_2$ nanotubes are employed as seeds to create 1D/2D heteroepitaxial MnO$_2$. The prepared α-MnO$_2$ nanotubes are reacted with an acidic KMnO$_4$ aqueous solution at 95 °C (see SI). Time-dependent experiments are performed to track the formation mechanism. Fig. S1 displays the morphology evolution at
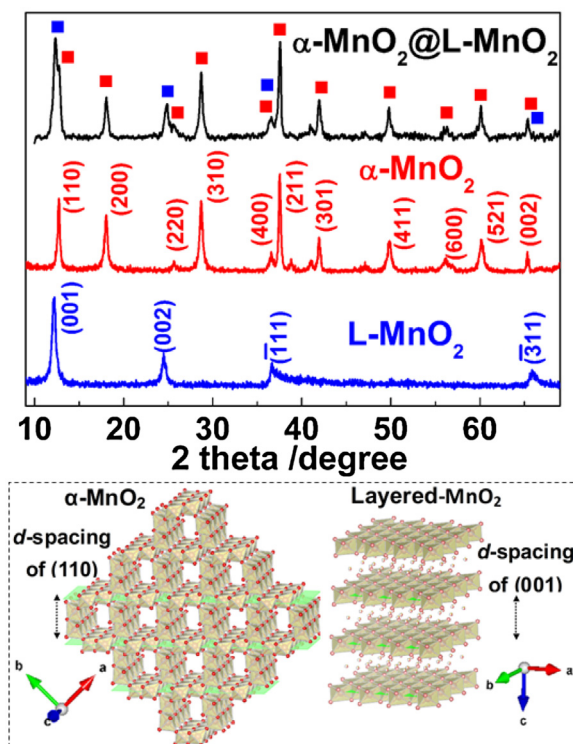

Fig. 1. The upper panel: powder XRD patterns of the prepared α-MnO$_2$ (JCPDS No. 44-0141), layered-MnO$_2$ (JCPDS No. 80-1098) and α-MnO$_2$@L-MnO$_2$. The below panel: schematic illustration of lattice match between α-MnO$_2$ and layered-MnO$_2$. Mn and O atoms are denoted as yellow and red balls, respectively. (For interpretation of the references to color in this figure legend, the reader is referred to the web version of this article.)

the initial 5 h. As can be seen, the smooth surface of the precursory nanotubes becomes branched, with formation of more branches at prolonged durations. After reaction for 1 h, some tiny branches start budding out from the surface of the nanotube stems. The tiny branches evolve into nanosheets after 5 h, with the growth
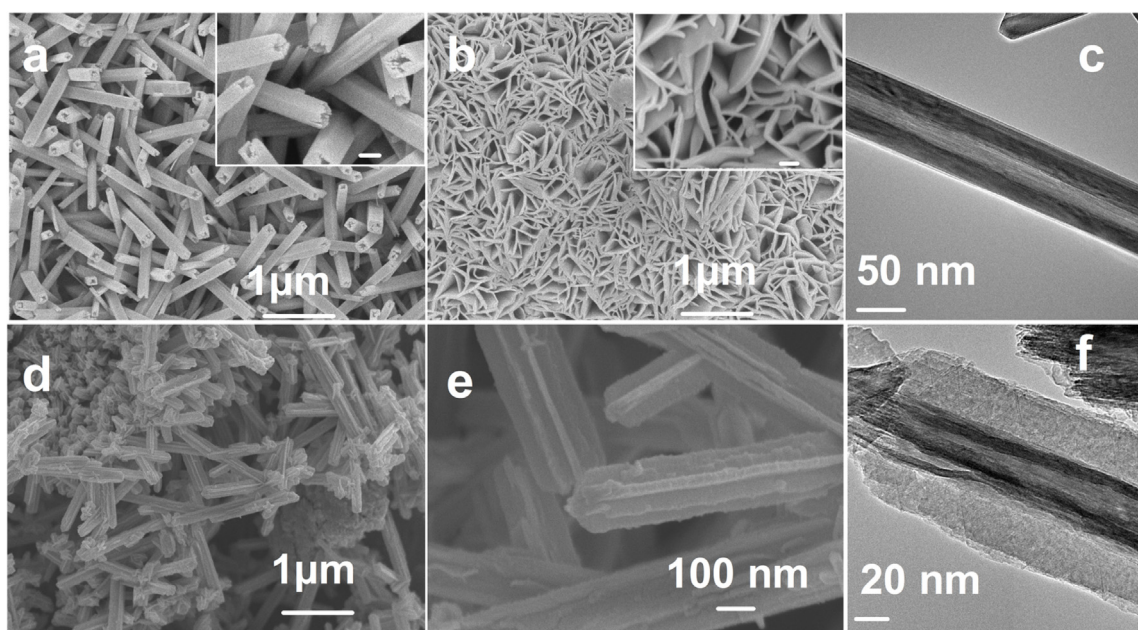
Fig. 2. FESEM (a, b, d and e) and TEM (c and f) images of the prepared α-MnO$_2$ (a and c), layered-MnO$_2$ (b) and α-MnO$_2$@L-MnO$_2$ (d, e and f). The scale bars in the insets are 100 nm.
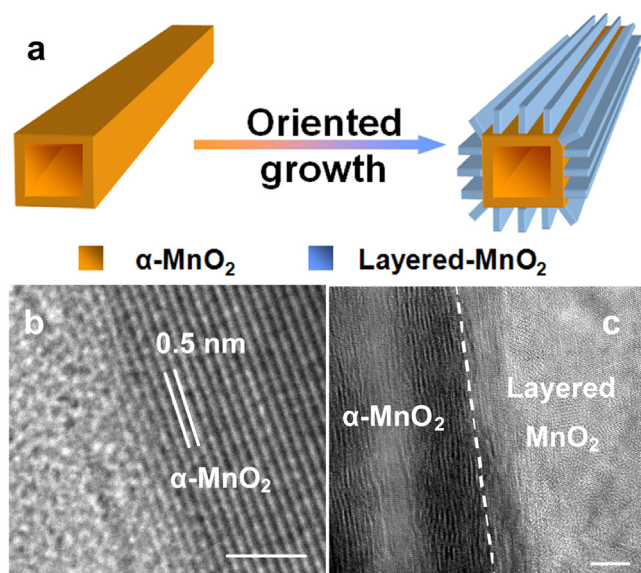
Fig. 3. (a) Schematic illustration of the proposed synthesis protocol; high-resolutionTEM images of the α-MnO$_2$ nanotubes (b) and α-MnO$_2$@L-MnO$_2$ (c). The scale bars are both 5 nm.

direction of the branched nanosheets being perpendicular to the longitudinal axis (c axis) of the nanotube seeds. The SEM and TEM images of the 12-h product are shown in Fig. 2d–f. Further prolonging the reaction to 12 h facilitates the continuous anisotropic growth of nanosheets in the shell, with formation of uniform hierarchical structures (Fig. 2d). The corresponding XRD pattern is shown in Fig. 1 (the upper panel). Besides the peaks assigned to the α-MnO$_2$ seeds (the red squares), peaks ascribed to layered MnO$_2$ clearly occur (the blue squares). The high-magnification SEM (Fig. 2e) and TEM (Fig. 2f) images clearly show that the successfully assembly of layered-MnO$_2$ nanosheets over the surface of α-MnO$_2$ seeds, consistent with Fig. 3a. Fig. 2f also suggests retention of nanotube architecture in the core. The above results evidently show the direct oriented growth of layered-MnO$_2$ nanosheets over α-MnO$_2$ nanotubes, in which the core-shell heterostructured α-MnO$_2$@L-MnO$_2$ can be tailored by varying the reaction time. During the oriented growth, the lateral size of the layered-MnO$_2$ nanosheets significantly increases. However, the thickness of the nanosheets still remains to be about 15 nm after 12 h growth.

The average Mn—O bond lengths of α-MnO$_2$ and layered-MnO$_2$ are 1.98 and 1.94 Å [49]. Such comparable Mn—O bonds facilitate the heteronucleation between the two phases. In the present case, the α-MnO$_2$ crystals serve as nuclei to assist the in-situ growth of layered MnO$_2$, leading to the formation of the unique α-MnO$_2$@L-MnO$_2$ core-shell heterostructures. The existed epitaxial relationship of $(110)(\alpha\text{-MnO}_2)\|(001)(\text{L-MnO}_2)$ facilitates the
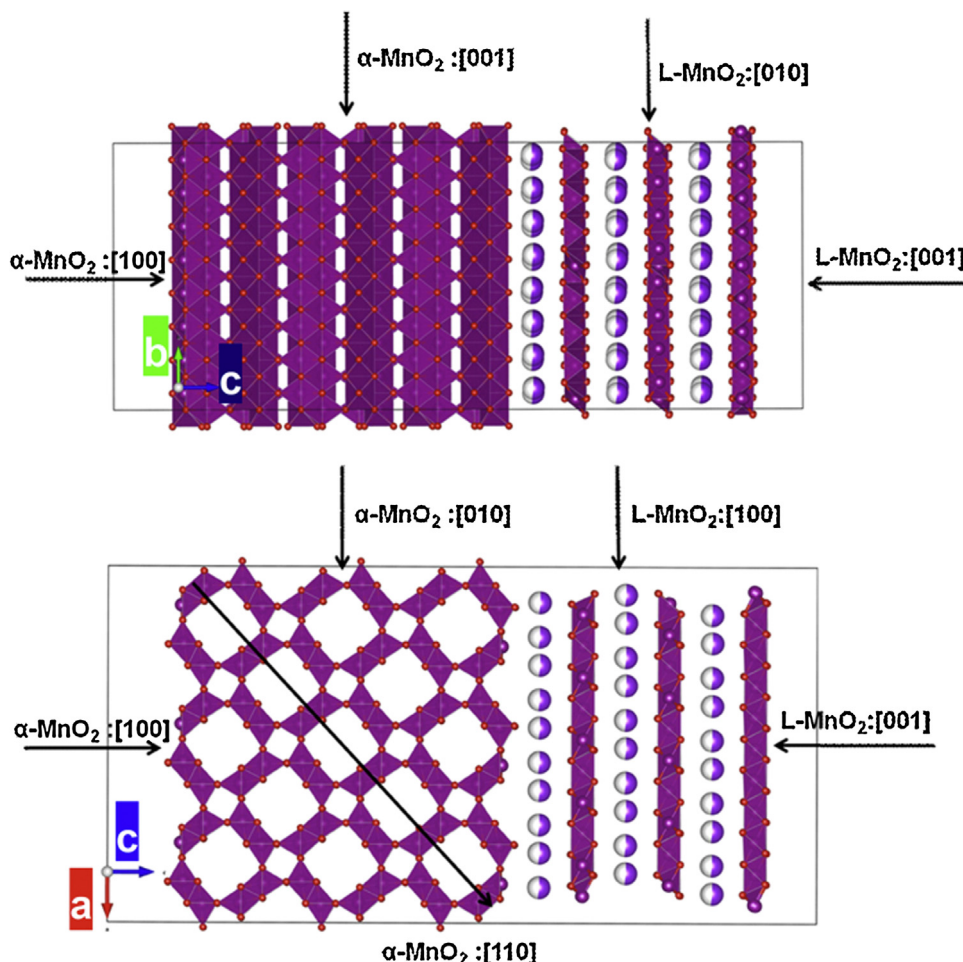
Fig. 4. Simulated crystallographic information of α-MnO$_2$ and layered MnO$_2$ (L-MnO$_2$) which are both placed in the same reference frame and in the same unit cell (in the rectangles). The purple and red balls represent Mn and O atoms, respectively. The balls filled with mixed colours represent cations (e.g. K$^+$ and/or H$_3$O$^+$) intercalated in the internal voids of the lattices. The used software is *Materials Studio* (version 7.0). (For interpretation of the references to color in this figure legend, the reader is referred to the web version of this article.)

formation of α-MnO$_2$@L-MnO$_2$ heteroepitaxy. Fig. 3b and c compares the surface of the α-MnO$_2$ nanobutes and heterointerface of the α-MnO$_2$@L-MnO$_2$. Fig. 3b shows that the α-MnO$_2$ nanobutes have smooth surface. A d-spacing of 0.5 nm ascribed to the spacing between (200) planes appears, which remains in the core of the α-MnO$_2$@L-MnO$_2$. As can be seen from Fig. 3c, a well-defined and coherent heterointerface occurs between the branched layered MnO$_2$ and backboned α-MnO$_2$.

The crystallographic compatibility between α-MnO$_2$ and L-MnO$_2$ phases is also demonstrated in Fig. 4. The {001} surface of L-MnO$_2$ phase is parallelly placed on the {100} surface of α-MnO$_2$ phase in the same reference frame and in the same unit cell. Generally, a stable heterointerface tends to be formed between two semiconductors with similar crystal features, especially unit cell parameter. The c parameter of α-MnO$_2$ unit cell is same with the b parameter of layered-MnO$_2$ unit cell. Hence, the [010] direction of L-MnO$_2$ would be parallel with the [001] direction of α-MnO$_2$ in the growth process of L-MnO$_2$. Moreover, both the two phases contain ordered voids in lattices (1D tunnels in α-MnO$_2$ and 2D interlayer gaps in L-MnO$_2$), in which cations such as K$^+$ and/or H$_3$O$^+$ are intercalated during synthesis [49]. As can be seen, such intercalated cations are capable of directly bridging the two phases, leading to formation of thermodynamically stable α-MnO$_2$@L-MnO$_2$ heteroepitaxy with well-defined interface by oriented growth.

3.2. Loading of Pt nanoparticles over the MnO$_2$ backbones

The prepared MnO$_2$ samples functions as backbones for trace Pt loading, with the content of Pt elements being controlled as 1 wt% in the precursors. Figs. 5 and S2 show the TEM images of the obtained Pt/α-MnO$_2$, Pt/α-MnO$_2$@L-MnO$_2$ and Pt/L-MnO$_2$. It is clearly seen that the morphology of the precursory MnO$_2$ remains after Pt loading. Figs. 5a, b and S2b show that nanoparticles are uni-
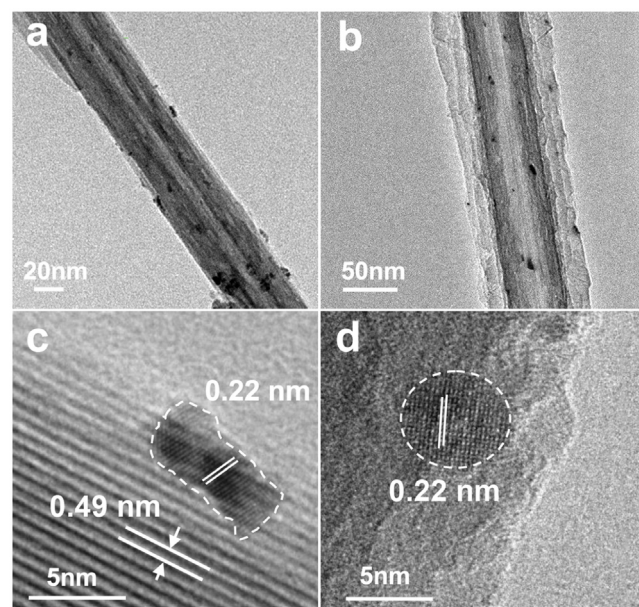

Fig. 5. TEM (a and b) and high-resolution TEM (c and d) images of the prepared Pt/α-MnO$_2$ (a and c) and Pt/α-MnO$_2$@L-MnO$_2$ (b and d).

formly dispersed on the surface of MnO$_2$, as indicated by the more black area. The high-resolution TEM images verify that the loaded nanoparticles are of diameters ranging from 3 to 5 nm. The lattice spacing of the coated nanoparticles is 0.22 nm, corresponding to lattice spacing of (111) planes of metallic Pt. The above results confirm the uniform loading of Pt nanoparticles over the MnO$_2$ backbones.
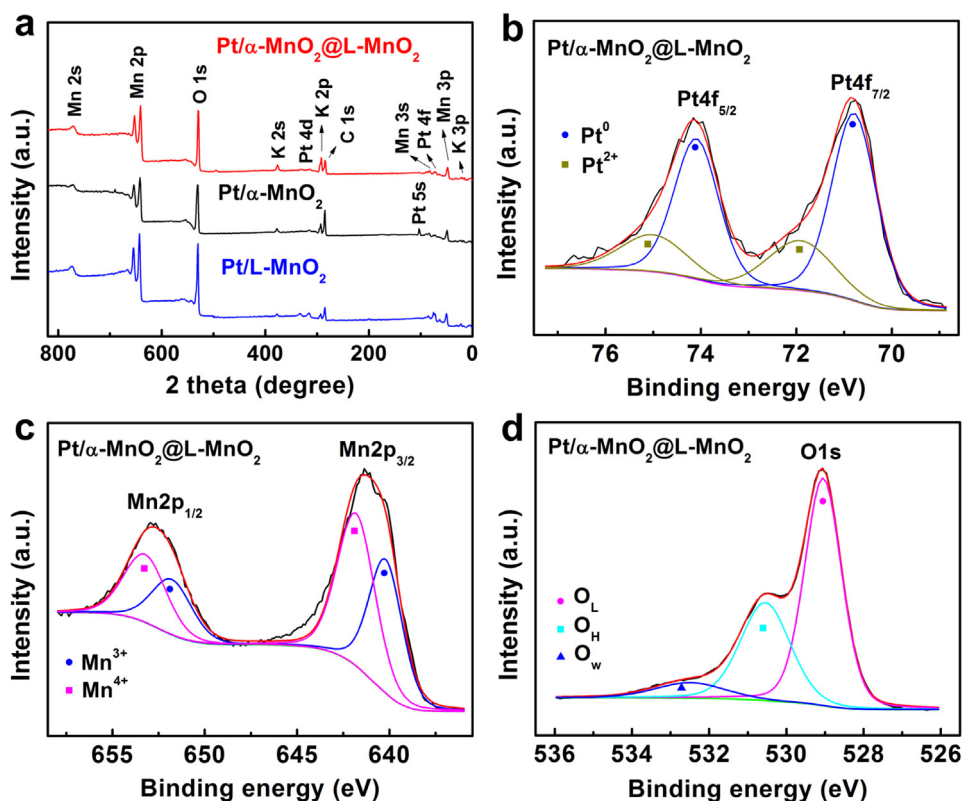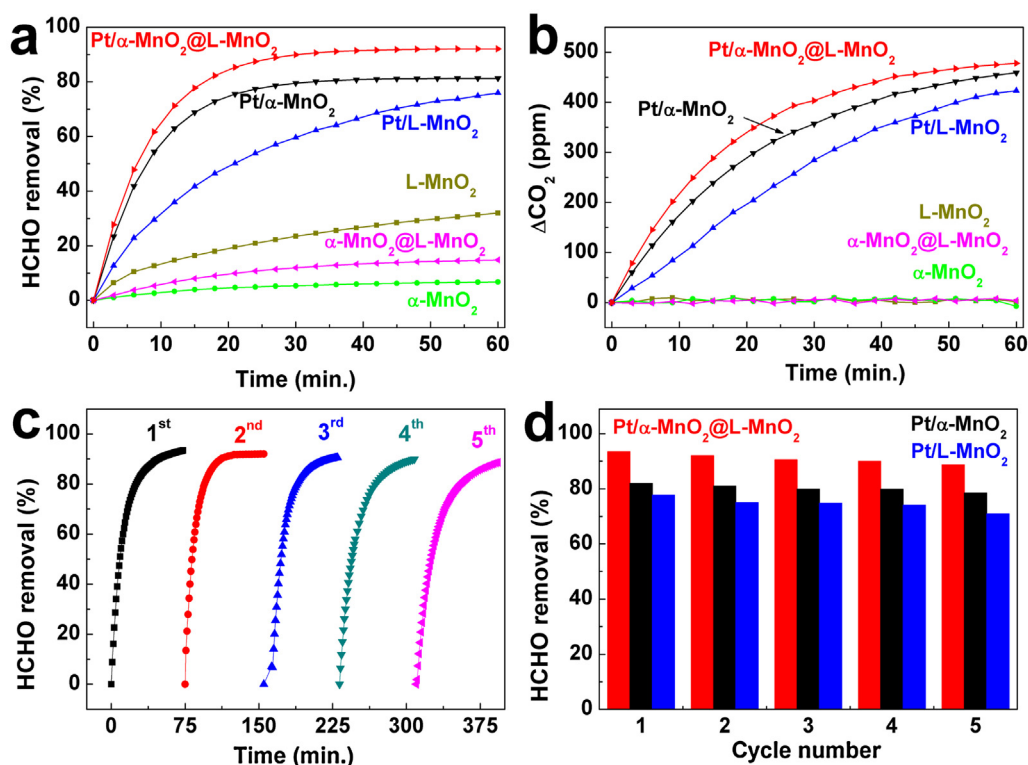

Fig. 6. XPS survey spectra of the Pt/α-MnO$_2$, Pt/L-MnO$_2$ and Pt/α-MnO$_2$@L-MnO$_2$ (a) and Pt 4f (b), Mn 2p (c) and O 1s (d) XPS spectra of the Pt/α-MnO$_2$@L-MnO$_2$.

Fig. 7. (a) HCHO removal capability of the samples; (b) changes of CO_2 concentrations during HCHO removal; (c) consecutive 5-cycle HCHO removal treatment of the $Pt/\alpha\text{-}MnO_2@L\text{-}MnO_2$; (d) comparison on the reusability of the samples. No generation measures were carried out.

3.3. Brunauere-Emmette-Teller (BET) and X-ray photoelectron spectroscopy (XPS) measurements

Brunauere-Emmette-Teller (BET) surface area and pore characteristics of the prepared $\alpha\text{-}MnO_2$ nanotubes, $\alpha\text{-}MnO_2@L\text{-}MnO_2$ (12 h) and $L\text{-}MnO_2$ were measured by using N_2 adsorption/desorption at 77 K. As can be seen in Fig. S3, the three isotherms are of type IV. Further observation indicates that both the hysteresis loops of the three samples are of typical H3 type, indicating the existence of narrow slit-shaped mesopores. The BET surface area and pore volume of the $\alpha\text{-}MnO_2@L\text{-}MnO_2$ (45 $m^2\,g^{-1}$) are significantly higher than those of the $\alpha\text{-}MnO_2$ nanotubes (25 $m^2\,g^{-1}$). The BET surface area of the $L\text{-}MnO_2$ is 63 $m^2\,g^{-1}$, the highest of the three MnO_2 samples.

Figs. 6, S4, S5 and S6 show the XPS data of the three Pt/MnO_2 data, with the data being summarized and compared in the corresponding tables. The survey XPS (Fig. 6a) suggests the co-existence of Mn, O, K and Pt in the three samples, with the content of Pt occurring in the range between 0.90 and 0.95 wt%. Such values are comparable with the stoichiometry in the precursors (i.e. 1.0 wt%).

In the Pt 4f spectra (Figs. 6b and S4), peak doublets ascribed to metallic Pt (Pt^0) and Pt^{2+} both appear. The content of Pt^0 is predominant, indicating the formation of metallic Pt and minor oxidation of Pt surface in air. The highest content of Pt^0 occurs in the $Pt/\alpha\text{-}MnO_2@L\text{-}MnO_2$, indicating retarded surface oxidization of the Pt nanoparticles in the sample.

Figs. 6c and S5 displays the Mn 2p spectra of the three Pt/MnO_2. The peaks of Mn 2p3/2 and 2p1/2 are centered at 641.1 and 652.9 eV. The corresponding spin-energy separation is 11.8 eV, indicating that the predominant oxidation state of Mn is 4+. It was reported that surface Mn^{4+} could provide oxygen vacancies [50]. Such surface oxygen vacancies are beneficial to adsorption and activation of oxygen [51]. The inset table for Fig. S4 exhibits the relative content of surface Mn^{4+} in the three samples, suggesting

the highest surface Mn^{4+} in the $Pt/\alpha\text{-}MnO_2$. Therefore, an enhanced oxygen adsorption appears in the $Pt/\alpha\text{-}MnO_2$ sample. This result agrees well with a previous report regarding the enhanced oxygen reduction capability of $\alpha\text{-}MnO_2$ than $L\text{-}MnO_2$, despite a higher BET surface area of the latter [49].
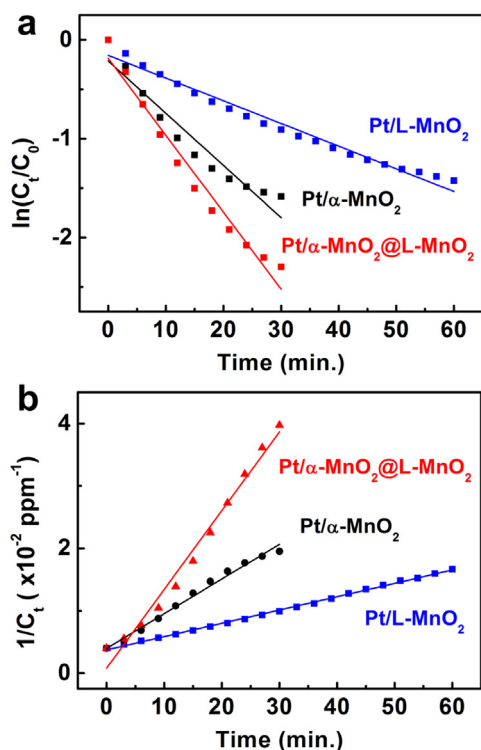
The O 1s spectra (Figs. 6d and S6) could be deconvolved into three peaks, assigned to lattice O species of MnO_2 (O_L), surface hydroxyl species (O_H) and chemically-bonded water (O_W). It was documented that O_H is beneficial to adsorption of HCHO [2–4]. The inserted table in Fig. S6 clearly shows that the $Pt/\alpha\text{-}MnO_2@L\text{-}MnO_2$ sample has the largest amount of O_H. Therefore, enhanced HCHO adsorption could be expected in the sample.

3.4. Room-temperature HCHO removal capability

Room-temperature HCHO removal capability of the pristine MnO_2 and the derived Pt/MnO_2 samples were measured in static conditions, with the concentrations of gaseous HCHO and CO_2 being online recorded. Fig. 7 displays and compares the variations between concentrations and treatment durations. For the pristine MnO_2 samples, the concentrations of HCHO decrease, with the concentrations of CO_2 remaining unchanged. This phenomenon suggests the HCHO adsorption instead of oxidization in the pristine MnO_2 samples. The HCHO removal ratios after 1 h are 31.9%, 6.7% and 14.8% for the $L\text{-}MnO_2$, $\alpha\text{-}MnO_2$ and $\alpha\text{-}MnO_2@L\text{-}MnO_2$, respectively. The HCHO adsorption tendency is in agreement with the order on specific surface area, suggesting an important role of surface area on adsorption. Besides surface area, surface chemistry also affects the HCHO adsorption. For materials with comparable surface area, introduction of surface hydroxyls could reduce the total energy of the HCHO adsorption system and provide the additional active centers for HCHO adsorption [2,4].

For the three Pt/MnO_2 samples, the decrease in HCHO concentrations and increase in CO_2 concentrations synchronically occur,

Fig. 8. First order (a) and second order (b) kinetic plot for the Pt/α-MnO$_2$, Pt/L-MnO$_2$ and Pt/α-MnO$_2$@L-MnO$_2$ samples.

Fig. 9. Optimized geometry structure of α-MnO$_2$ {100} surface: front view (a) and oblique view (b). The darkmagenta and red spheres represent Mn (larger) and O atoms (smaller). The calculated surface energy is 1.31 J m^{-2}. (For interpretation of the references to color in this figure legend, the reader is referred to the web version of this article.)

verifying the effective HCHO oxidation based on Reaction (1). The HCHO removal ratios after 1 h are 75.9%, 81.3% and 92.1% for the Pt/L-MnO$_2$, Pt/α-MnO$_2$ and Pt/α-MnO$_2$@L-MnO$_2$, respectively. The HCHO removal and CO$_2$ augment both follow the order: Pt/α-MnO$_2$@L-MnO$_2$ > Pt/α-MnO$_2$ > Pt/L-MnO$_2$. Such a tendency contradicts with the order on specific surface area, indicating a more important role of surface chemistry than surface area on room-temperature HCHO oxidation.
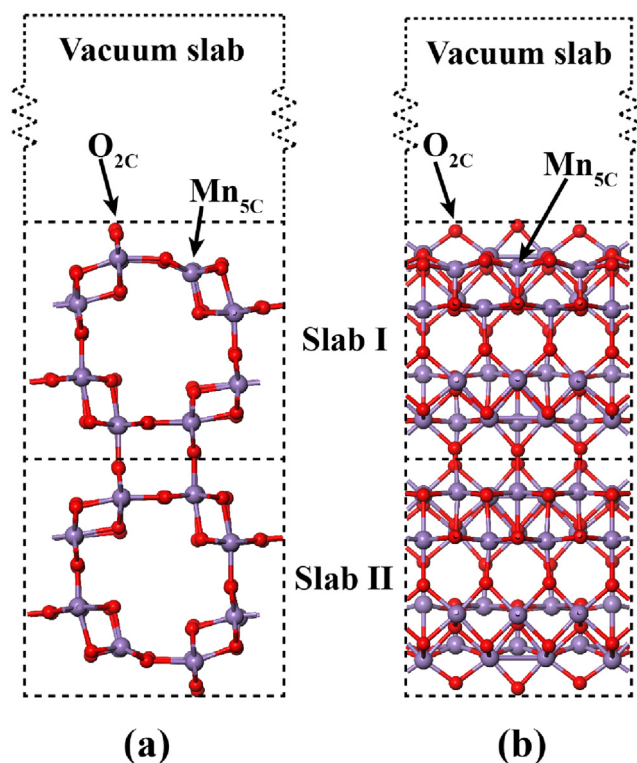
According to the overall reaction (as represented in Reaction (1)), CO$_2$ is generated at the expense of equal moles of HCHO. Theoretically, increase in CO$_2$ amount is equal with that of HCHO decrease. Commercial HCHO solutions generally contain 10–15% methanol as stabilizer to prevent polymerization (See the experimental section for details). Therefore, the presence of methanol in the reaction box is inevitable. The present methanol could also be oxidized into CO$_2$. Therefore, higher amounts of CO$_2$ increase than that of HCHO decrease appears in practical experiments (shown in Fig. 7a and b). Such a phenomenon also occurs in many references [22,24]. Due to this phenomenon, variation on HCHO concentrations instead of CO$_2$ concentrations is utilized to analyze the reaction kinetics.

To further study the kinetics of the oxidation, two most widely applied kinetic models, i.e., the first order and second order models were used to fit the reaction data. The first order and second order equations are presented as the Eqs. (2) and (3):
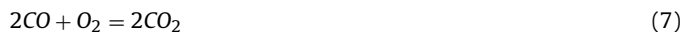
$$\ln \frac{C_t}{C_0} = -k_1 t \tag{2}$$

$$\frac{1}{C_t} - \frac{1}{C_0} = k_2 t \tag{3}$$

where t (min) is the treatment time; C_0 (ppm) and C_t (ppm) is the concentration of HCHO at $t = 0$ (min) and time t (min); and k_1 (min^{-1}) and k_2 (ppm^{-1} min^{-1}) are the rate constants derived from the first order and second order kinetics.

The three plots of HCHO removal against treatment time were analyzed with the first order and second order models, respectively. As can be seen from Fig. 8, the HCHO removal kinetics follows the second order kinetic model. The reaction mechanism is an important but complicated issue. The reported mechanisms are contradictory in details, even for the comparable materials. Formate [27] and CO [28] were separately reported as the intermediates for the same catalysts, Pt/TiO$_2$. The two kinds of intermediate represent two different reaction pathways (the Reaction (4)–(5) vs. Reaction (6)–(7)).

$$2HCHO + O_2 = 2HCOOH \tag{4}$$

$$2HCOOH + O_2 = 2CO_2 + 2H_2O \tag{5}$$

$$2HCHO + O_2 = 2CO + 2H_2O \tag{6}$$

$$2CO + O_2 = 2CO_2 \tag{7}$$

Although contradiction remains in the detailed pathways, it is well accepted that the activation of oxygen is the key step for the overall HCHO catalytic oxidation [1]. In this regard, the Reactions (4) or (6) are the rate-determining steps. In the static experiments, the activity (or partial pressure) of O$_2$ is several orders of magnitude higher than that of HCHO. The activity of O$_2$ is hence regarded as unchanged. Therefore, the rate law expression for either the Reactions (4) or (6) follows:

$$R = k_2 [HCHO]^2 \tag{8}$$

As indicated in the Eq. (8), the reaction kinetics is second order with respect to HCHO, agreeing well the fitting results. The derived rate constants are 1.26×10^{-3}, 5.55×10^{-4} and 2.13×10^{-4} ppm^{-1} min^{-1} for the Pt/α-MnO$_2$@L-MnO$_2$, Pt/α-MnO$_2$, Pt/L-MnO$_2$. Despite the largest specific surface area, the Pt/L-MnO$_2$
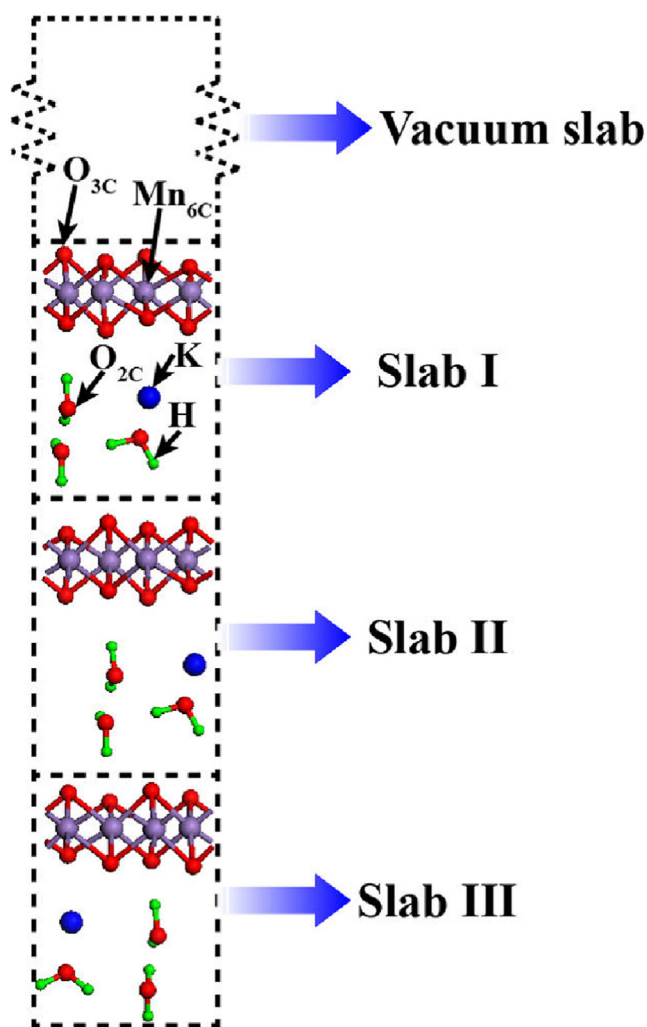
Fig. 10. Optimized geometry structure of layered-MnO$_2$ {001} surface. The dark magenta, red, blue and green spheres represent Mn, O, K and H atoms. The calculated surface energy is 0.11 J m^{-2}. (For interpretation of the references to color in this figure legend, the reader is referred to the web version of this article.)

shows the lowest rate constant. And the rate constant of the Pt/α-MnO$_2$@L-MnO$_2$ exceeds that of the Pt/α-MnO$_2$ and the Pt/L-MnO$_2$ by 2.27 and 5.92 times.

The reproducibility of the Pt/MnO$_2$ samples was measured without any generations. As shown in Fig. 7c and d, the retention ratios on HCHO removal capacity after 5-time consecutive treatment cycles remains as high as 94.96%, 95.77% and 91.41% for the Pt/α-MnO$_2$@L-MnO$_2$, Pt/α-MnO$_2$, Pt/L-MnO$_2$. This result highlights the excellent cycling stability of the samples. The stability tendency follows the reverse order on their specific surface area, indicating that excessively high surface area tends to deteriorate the reproducibility. According to a recent review [1], the origins for degradation of catalysts remains far from well specified. The deactivation of catalysts is mainly due to alternation of surface chemistry of catalyst upon HCHO oxidation. Therefore, samples with higher surface area tend to show higher degradation, due to the high surface energy. Upon treatment, precious metal particles might be irreversibly oxidized, which might retard activation of oxygen. This poisoning effect was demonstrated with the reduced Pd catalyst being much more active than the oxidized Pd catalyst in the catalytic oxidation of HCHO at room temperature [52]. The sluggish kinetics for desorption of intermediates (HCOOH and CO) and resultants (water) might also cause deactivation of catalysts. Last but not the least, the introduction of impurities over the surface of catalysts contributes to activity fading, as evidenced by the poisoning effect of molecules containing halogen or sulfur with excessively strong bonding capability to cations or metal atoms of catalysts [1,28].

3.5. Rationalization on the room-temperature HCHO removal capability

The above results confirm that the Pt/α-MnO$_2$@L-MnO$_2$ possesses enhanced room-temperature catalytic oxidation of gaseous HCHO in terms of HCHO removal capacity and kinetics. The XPS suggests the most abundant surface hydroxyl on the Pt/α-MnO$_2$@L-MnO$_2$, beneficial to adsorption of HCHO. More oxygen vacancies in α-MnO$_2$ than L-MnO$_2$, and the higher surface area of the Pt/α-MnO$_2$@L-MnO$_2$ than the Pt/α-MnO$_2$ account for the superior catalytic capability of the Pt/α-MnO$_2$@L-MnO$_2$.

Morphology observations (Figs. 2, 3 and 5) clearly show that the prepared samples have well-defined geometry. The exposed facets of the samples are then analyzed since surface chemistry plays a vital role on catalytic capability. The α-MnO$_2$ nanotubes only have exposed facets of α-MnO$_2$ {100} surface. And the L-MnO$_2$ nanosheets have sole exposed facets of layered-MnO$_2$ {001} surface. While the α-MnO$_2$@L-MnO$_2$ shows the exposed facets of the both forenamed surfaces.

To further elucidate the surface chemistry of the samples, Density-Functional-Theory (DFT) calculations were performed to investigate the effect of exposed crystal facet on surface chemistry of α-MnO$_2$ {100} surface and layered-MnO$_2$ {001} surface. For thermal catalytic oxidation of HCHO, non-precious materials only show appreciable catalytic capability at temperature higher than 80 °C [20,21,23,25,26,31]. Only loading with trace precious metals (Pt, Au, Ag and Pd), room-temperature catalytic oxidation of HCHO becomes possible [1,8,9,11,12,14,16,17,24,27,43,44]. It is then speculated and assumed that the loaded Pt is beneficial to desorption of generated water. Such an assumption agrees well with a recent paper regarding room-temperature HCHO oxidation over Pt/TiO$_2$ [28].

The amount of Pt, dispersion of Pt over MnO$_2$, particle size of Pt and surface chemistry of Pt impose influence of HCHO oxidation. In the present study, comparable amounts (0.9–0.95 wt%) of Pt were loaded on different MnO$_2$ matrix and the particle size of loaded Pt is comparable (3–5 nm). For construction of structural models, it is a high challenge for us to incorporate loaded Pt nanoparticles. Therefore, the DFT simulations herein only involves in the MnO$_2$ matrix. We acknowledge that the influence of loaded Pt is important and such influence deserves further detailed study in future.

The Pt 4f XPS spectra (Figs. 6b and S4) give some hints on the intercalation between Pt and MnO$_2$ matrix. Pt nanoparticles generally show excessively strong affinity towards oxygen, with inevitable formation of Pt-O over the outer surface of Pt nanoparticles. The surface Pt-O might deteriorate the catalytic performance of Pt nanoparticles. As can be seen, the lowest content of Pt-O appears in the Pt/α-MnO$_2$@L-MnO$_2$ sample. This result indicates strong interaction between the Pt and the α-MnO$_2$@L-MnO$_2$, which deserves further study in future.

As shown in Fig. 9, α-MnO$_2$ {100} surface is terminated by two-coordination O (O$_{2C}$) and five-coordination Mn (Mn$_{5C}$) atoms. Both the two kinds of configuration are unsaturated, indicating high bonding ability of the surface. It is also noted that the α-MnO$_2$ {100} surface is a typical high-energy surface with a surface energy (E_S) as high as 1.31 J m^{-2}.

In comparison, the layered-MnO$_2$ {001} surface is terminated by the three-coordination O (O$_{3C}$) atoms (see Fig. 10). Besides, all Mn atoms in the O—Mn—O layer are six-coordination (Mn$_{6C}$). There is no unsaturated Mn atom exposed in layered-MnO$_2$ {001} surface. The calculated E_S of layered-MnO$_2$ {001} surface is only 0.11 J m^{-2}.
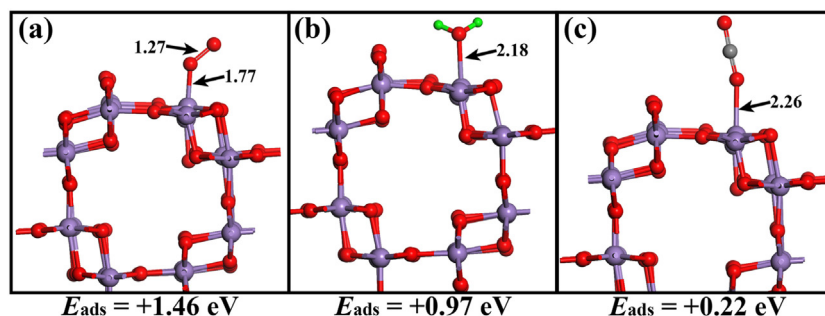
Fig. 11. Adsorptions of O_2 (a), H_2O (b) and CO_2 (c) on the Mn_{5C} atom of α-MnO_2 {100} surface. The black numbers pointing to atoms stand for the bond lengths (Å). The darkmagenta, red, green and grey spheres represent Mn, O, H and C atoms. The black numbers pointing to bonds stand for the bond lengths (Å). (For interpretation of the references to color in this figure legend, the reader is referred to the web version of this article.)
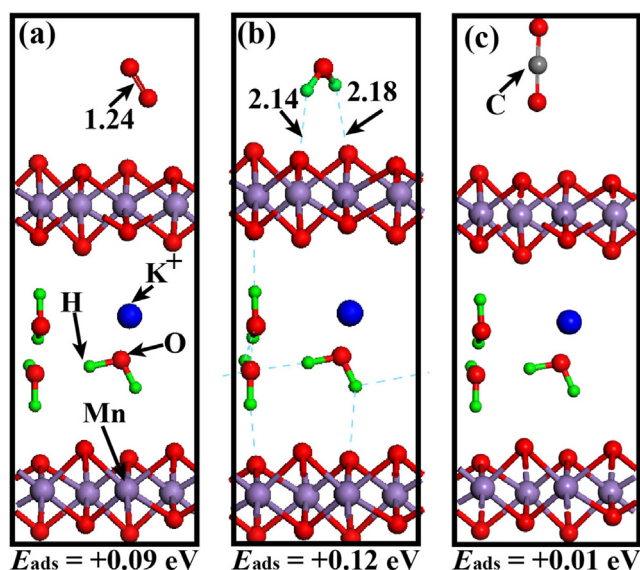
Fig. 12. Adsorption of O_2 (a), H_2O (b) and CO_2 (c) on the {001} surface of layered-MnO_2. The black number pointing to bond stands for the bond length (Å). The darkmagenta, red, blue, green and grey spheres represent Mn, O, K, H and C atoms. (For interpretation of the references to color in this figure legend, the reader is referred to the web version of this article.)

Therefore, the layered-MnO_2 {001} surface has low surface energy and low bonding ability.

The difference on surface energy, utmost atomic configuration and bonding capability of the two facets are well-reflected in their discrepant adsorption of gaseous O_2 and H_2O. The unsaturated atoms in utmost surface, high surface energy and excellent bonding ability of α-MnO_2 {100} surface render stable chemisorptions of O_2 and H_2O, with the calculated adsorption energies (E_{ads}) being as high as 1.46 and 0.97 eV (Fig. 11). Especially, the Mn—O bond formed between O_2 and Mn_{5C} atom effectively promotes the transfer of more electrons from α-MnO_2 {100} surface to O_2 (see Fig. 11a). As a result, the O_2 bonded to the Mn_{5C} atom has the highest reduction degree and the long O—O bond (1.27 Å). Hence, it is concluded that O_2 can be easily activated and reduced on α-MnO_2 {100} surface.

In contrast, O_2 and H_2O molecules can only be physisorbed on layered-MnO_2 {001} surface, incurring the E_{ads} being as low as 0.09 and 0.12 eV for adsorption of O_2 and H_2O (Fig. 12). Due to the weak physisorption, the absorbed O_2 and H_2O remain their un-activated states. For instance, the bond length of O_2 physisorbed on layered-MnO_2 {001} surface (1.24 Å) is smaller than that of chemisorbed on α-MnO_2 {100} surface (1.27 Å).

For layered MnO_2, cations (e.g. K^+) and chemically bonded water could intercalate into the interlayer gaps during preparation and/or

Table 1
First order and second order kinetics parameters.

	First order		Second order	
	k_1 (min^{-1})	R^2	k_2 (ppm^{-1} min^{-1})	R^2
Pt/L-MnO_2	0.02295	0.97546	2.13015×10^{-4}	0.99829
Pt/α-MnO_2	0.05279	0.92747	5.54636×10^{-4}	0.98861
Pt/α-MnO_2@L-MnO_2	0.07777	0.96855	1.26000×10^{-3}	0.98167

processing. The intercalated K^+ might change catalytic capability of layered MnO_2. A recent publication suggests that the intercalation of K^+ results in higher manganese vacancies and better HCHO decomposition [23]. DFT simulations on the layered-MnO_2 without intercalated K^+ are herein performed. As shown in Fig. S7, the intercalated K^+ makes no change on the surface energy (e.g. 0.11 J m^{-2}), utmost atomic configuration (O_{3C} and Mn_{6C}) and bonding capability (0.12 eV for adsorption of H_2O) of layered MnO_2. This result confirms that intercalated K^+ plays no influence of the reaction thermodynamics. However, the intercalated K^+ might affect reaction kinetics, which deserves further detailed investigation in future (Table 1).

Strong adsorption of reactants and weak adsorption of resultants over catalysts are favorable for a catalytic reaction. As shown in Figs. 11 and 12, the adsorption of CO_2 over the both facets are physical adsorption, with very small adsorption energy of 0.22 and 0.01 eV occurring in the α-MnO_2 {100} surface and {001} surface of layered-MnO_2. In particular, the adsorption energy of CO_2 is much lower than that of O_2 and H_2O. It is then rational to conclude that the desorption of the resulting CO_2 can hardly be the rate-determining step.

The α-MnO_2 has strong adsorption of both O_2 (reactant) and H_2O (resultant), with desorption of H_2O being the kinetic barriers for Reaction (1). The L-MnO_2 shows weak adsorption of both O_2 and H_2O, in which weak adsorption and activation of O_2 retard Reaction (1). In the α-MnO_2@L-MnO_2 heteroepitaxy, the exposed α-MnO_2 {100} surface facilitates adsorption and activation of O_2, and the exposed layered-MnO_2 {001} surface is beneficial to desorption of resultant H_2O. Upon such the synergetic combination, room-temperature oxidation of HCHO to CO_2 and H_2O is significantly enhanced.

The strong reactivity of the rationally designed α-MnO_2@L-MnO_2 is also reflected by the enhanced electrocatalytic activity towards the Oxygen Reduction Reaction (ORR). As shown in Fig. S8, the L-MnO_2 displays the lowest ORR activity (the smallest current and the most negative onset potential for ORR), despite the highest BET surface area of the sample. Due to the strong affinity towards O_2 (reactants) of the exposed facet of the α-MnO_2, the sample shows much enhanced ORR activity to the L-MnO_2. By construction of α-MnO_2@L-MnO_2, both the adsorption of reactants and desorption of resultants/intermediates are facilitated, resulting in the highest

ORR activity of the α-MnO$_2$@L-MnO$_2$. The present study highlights the rational design protocols on integrating well-defined strong adsorption/weak adsorption heteroepitaxy for advanced catalysis for diverse energy and environmental applications.

4. Conclusions

In summary, core-shell α-MnO$_2$@L-MnO$_2$ heteroepitaxy with α-MnO$_2$ nanotubes as the core and layered-MnO$_2$ as the shell was constructed through oriented growth of layered-MnO$_2$ nanosheets (L-MnO$_2$) over α-MnO$_2$ nanotubes. By simply varying the duration of oriented growth, the dimensions of the shelled layered MnO$_2$ could be tailored. The epitaxial relationship in the heteroepitaxy is rationalized as (110)(α-MnO$_2$)||(001)(L-MnO$_2$). Trace Pt nanoparticles (1 wt%) were uniformly coated over the MnO$_2$ samples and the resulting Pt/MnO$_2$ samples were evaluated as catalysts for room-temperature gaseous HCHO oxidation. The Pt/α-MnO$_2$@L-MnO$_2$ displayed higher HCHO removal capacity and enhanced kinetics, compared to the Pt/α-MnO$_2$ and Pt/L-MnO$_2$. DFT simulations clearly show that α-MnO$_2$ {100} surface facilitates adsorption and activation of O$_2$, and the exposed layered-MnO$_2$ {001} surface is beneficial to desorption of resultant H$_2$O. The α-MnO$_2$@L-MnO$_2$ heteroepitaxy simultaneously integrates exposed facets of α-MnO$_2$ {100} surface and layered-MnO$_2$ {001} surface, in which the synergetic effect of the two surfaces leads to significantly enhanced room-temperature HCHO oxidation activity. The present study provides a facile and effective strategy for construction of well-defined 1D/2D heteroepitaxy and a rational design of manganese oxide-based catalysts for advanced environmental and energy applications (e.g. oxygen reduction).

Acknowledgements

Appendix A. Supplementary data

Supplementary data associated with this article can be found, in the online version, at http://dx.doi.org/10.1016/j.apcatb.2017.01.083.

References

[1] L. Nie, J. Yu, M. Jaroniec, F.F. Tao, Room-temperature catalytic oxidation of formaldehyde on catalysts, Catal. Sci. Technol. 6 (2016) 3649–3669.

[2] J.G. Yu, X.Y. Li, Z.H. Xu, W. Xiao, NaOH-modified ceramic honeycomb with enhanced formaldehyde adsorption and removal performance, Environ. Sci. Technol. 47 (2013) 9928–9933.

[3] Z. Xu, J. Yu, W. Xiao, Microemulsion-assisted preparation of a mesoporous ferrihydrite/SiO$_2$ composite for the efficient removal of formaldehyde from air, Chem.-Eur. J. 19 (2013) 9592–9598.

[4] P. Zhou, X.F. Zhu, J.G. Yu, W. Xiao, Effects of adsorbed F, OH, and Cl ions on formaldehyde adsorption performance and mechanism of anatase TiO$_2$ nanosheets with exposed {001} facets, ACS Appl. Mater. Interfaces 5 (2013) 8165–8172.

[5] W.-J. Liang, J. Li, J.-X. Li, T. Zhu, Y.-Q. Jin, Formaldehyde removal from gas streams by means of NaNO$_2$ dielectric barrier discharge plasma, J. Hazard. Mater. 175 (2010) 1090–1095.

[6] X. Zhu, X. Gao, R. Qin, Y. Zeng, R. Qu, C. Zheng, X. Tu, Plasma-catalytic removal of formaldehyde over Cu–Ce catalysts in a dielectric barrier discharge reactor, Appl. Catal. B-Environ. 170–171 (2015) 293–300.

[7] N. Lu, J. Pei, Y. Zhao, R. Qi, J. Liu, Performance of a biological degradation method for indoor formaldehyde removal, Build. Environ. 57 (2012) 253–258.

[8] X. Tang, J. Chen, X. Huang, Y. Xu, W. Shen, Pt/MnO$_x$–CeO$_2$ catalysts for the complete oxidation of formaldehyde at ambient temperature, Appl. Catal. B-Environ. 81 (2008) 115–121.

[9] Y. Chen, J. He, H. Tian, D. Wang, Q. Yang, Enhanced formaldehyde oxidation on Pt/MnO$_2$ catalysts modified with alkali metal salts, J. Colloid Interface Sci. 428 (2014) 1–7.

[10] L. Liu, H. Tian, J. He, D. Wang, Q. Yang, Preparation of birnessite-supported Pt nanoparticles and their application in catalytic oxidation of formaldehyde, J. Environ. Sci. 24 (2012) 1117–1124.

[11] X. Yu, J. He, D. Wang, Y. Hu, H. Tian, T. Dong, Z. He, Au–Pt bimetallic nanoparticles supported on nest-like MnO$_2$: synthesis and application in HCHO decomposition, J. Nanopart. Res. 14 (2012) 1260.

[12] X. Yu, J. He, D. Wang, Y. Hu, H. Tian, Z. He, Facile controlled synthesis of Pt/MnO$_2$ nanostructured catalysts and their catalytic performance for oxidative decomposition of formaldehyde, J. Phys. Chem. C 116 (2012) 851–860.

[13] J. Wang, D. Li, P. Li, P. Zhang, Q. Xu, J. Yu, Layered manganese oxides for formaldehyde-oxidation at room temperature: the effect of interlayer cations, RSC Adv. 5 (2015) 100434–100442.

[14] L. Nie, J. Yu, X. Li, B. Cheng, G. Liu, M. Jaroniec, Enhanced performance of NaOH-modified Pt/TiO$_2$ toward room temperature selective oxidation of formaldehyde, Environ. Sci. Technol. 47 (2013) 2777–2783.

[15] X. Tang, J. Chen, Y. Li, Y. Li, Y. Xu, W. Shen, Complete oxidation of formaldehyde over Ag/MnO$_x$–CeO$_2$ catalysts, Chem. Eng. J. 118 (2006) 119–125.

[16] Y. Shen, X. Yang, Y. Wang, Y. Zhang, H. Zhu, L. Gao, M. Jia, The states of gold species in CeO$_2$ supported gold catalyst for formaldehyde oxidation, Appl. Catal. B-Environ. 79 (2008) 142–148.

[17] C. Zhang, F. Liu, Y. Zhai, H. Ariga, N. Yi, Y. Liu, K. Asakura, M. Flytzani-Stephanopoulos, H. He, Alkali-metal-promoted Pt/TiO$_2$ opens a more efficient pathway to formaldehyde oxidation at ambient temperatures, Angew. Chem. Int. Ed. 51 (2012) 9628–9632.

[18] B. Bai, Q. Qiao, H. Arandiyan, J. Li, J. Hao, Three-dimensional ordered mesoporous MnO$_2$-supported Ag nanoparticles for catalytic removal of formaldehyde, Environ. Sci. Technol. 50 (2016) 2635–2640.

[19] L. Ma, D.S. Wang, J.H. Li, B.Y. Bai, L.X. Fu, Y.D. Li, Ag/CeO$_2$ nanospheres: efficient catalysts for formaldehyde oxidation, Appl. Catal. B-Environ. 148 (2014) 36–43.

[20] L. Lu, H. Tian, J. He, Q. Yang, Graphene–MnO$_2$ hybrid nanostructure as a new catalyst for formaldehyde oxidation, J. Phys. Chem. C 120 (2016) 23660–23668.

[21] Y. Huang, B. Long, M. Tang, Z. Rui, M.-S. Balogun, Y. Tong, H. Ji, Bifunctional catalytic material: an ultrastable and high-performance surface defect CeO$_2$ nanosheets for formaldehyde thermal oxidation and photocatalytic oxidation, Appl. Catal. B-Environ. 181 (2016) 779–787.

[22] Z. Xu, J. Yu, M. Jaroniec, Efficient catalytic removal of formaldehyde at room temperature using AlOOH nanoflakes with deposited Pt, Appl. Catal. B-Environ. 163 (2015) 306–312.

[23] J. Wang, J. Li, C. Jiang, P. Zhou, P. Zhang, J. Yu, The effect of manganese vacancy in birnessite-type MnO$_2$ on room-temperature oxidation of formaldehyde in air, Appl. Catal. B-Environ. 204 (2017) 147–155.

[24] Z. Yan, Z. Xu, J. Yu, M. Jaroniec, Enhanced formaldehyde oxidation on CeO$_2$/AlOOH-supported Pt catalyst at room temperature, Appl. Catal. B-Environ. 199 (2016) 458–465.

[25] J. Zhang, Y. Li, L. Wang, C. Zhang, H. He, Catalytic oxidation of formaldehyde over manganese oxides with different crystal structures, Catal. Sci. Technol. 5 (2015) 2305–2313.

[26] Y. Wang, X. Zhu, M. Crocker, B. Chen, C. Shi, A comparative study of the catalytic oxidation of HCHO and CO over Mn$_{0.75}$Co$_{2.25}$O$_4$ catalyst: the effect of moisture, Appl. Catal. B-Environ. 160–161 (2014) 542–551.

[27] D.W. Kwon, P.W. Seo, G.J. Kim, S.C. Hong, Characteristics of the HCHO oxidation reaction over Pt/TiO$_2$ catalysts at room temperature: the effect of relative humidity on catalytic activity, Appl. Catal. B-Environ. 163 (2015) 436–443.

[28] P. Zhou, J. Yu, L. Nie, M. Jaroniec, Dual-dehydrogenation-promoted catalytic oxidation of formaldehyde on alkali-treated Pt clusters at room temperature, J. Mater. Chem. A 3 (2015) 10432–10438.

[29] J.G. Yu, S.H. Wang, J.X. Low, W. Xiao, Enhanced photocatalytic performance of direct Z-scheme g-C$_3$N$_4$-TiO$_2$ photocatalysts for the decomposition of formaldehyde in air, Phys. Chem. Chem. Phys. 15 (2013) 16883–16890.

[30] I. Jansson, S. Suárez, F.J. Garcia-Garcia, B. Sánchez, Zeolite–TiO$_2$ hybrid composites for pollutant degradation in gas phase, Appl. Catal. B-Environ. 178 (2015) 100–107.

[31] G. Wang, B. Huang, Z. Lou, Z. Wang, X. Qin, X. Zhang, Y. Dai, Valence state heterojunction Mn$_3$O$_4$/MnCO$_3$: photo and thermal synergistic catalyst, Appl. Catal. B-Environ. 180 (2016) 6–12.

[32] Q. Kuang, Z.Y. Jiang, Z.X. Xie, S.C. Lin, Z.W. Lin, S.Y. Xie, R.B. Huang, L.S. Zheng, Tailoring the optical property by a three-dimensional epitaxial heterostructure: a case of ZnO/SnO$_2$, J. Am. Chem. Soc. 127 (2005) 11777–11784.

[33] Y.J. Gong, S.D. Lei, G.L. Ye, B. Li, Y.M. He, K. Keyshar, X. Zhang, Q.Z. Wang, J. Lou, Z. Liu, R. Vajtai, W. Zhou, P.M. Ajayan, Two-step growth of two-dimensional WSe$_2$/MoSe$_2$ heterostructures, Nano Lett. 15 (2015) 6135–6141.

[34] L.L. Xu, X.L. Sun, H. Tu, Q. Jia, H.T. Gong, J.G. Guan, Synchronous etching-epitaxial growth fabrication of facet-coupling NaTaO$_3$/Ta$_2$O$_5$ heterostructured nanofibers for enhanced photocatalytic hydrogen production, Appl. Catal. B-Environ. 184 (2016) 309–319.

[35] X.D. Duan, C. Wang, J.C. Shaw, R. Cheng, Y. Chen, H.L. Li, X.P. Wu, Y. Tang, Q.L. Zhang, A.L. Pan, J.H. Jiang, R.Q. Yu, Y. Huang, X.F. Duan, Lateral epitaxial

growth of two-dimensional layered semiconductor heterojunctions, Nat. Nanotechnol. 9 (2014) 1024–1030.

[36] L.J. Lauhon, M.S. Gudiksen, C.L. Wang, C.M. Lieber, Epitaxial core-shell and core-multishell nanowire heterostructures, Nature 420 (2002) 57–61.

[37] A.Y. Borisevich, H.J. Chang, M. Huijben, M.P. Oxley, S. Okamoto, M.K. Niranjan, J.D. Burton, E.Y. Tsymbal, Y.H. Chu, P. Yu, R. Ramesh, S.V. Kalinin, S.J. Pennycook, Suppression of octahedral tilts and associated changes in electronic properties at epitaxial oxide heterostructure interfaces, Phys. Rev. Lett. 105 (2010).

[38] C.N. Van, W.S. Chang, J.W. Chen, K.A. Tsai, W.Y. Tzeng, Y.C. Lin, H.H. Kuo, H.J. Liu, K.D. Chang, W.C. Chou, C.L. Wu, Y.C. Chen, C.W. Luo, Y.J. Hsu, Y.H. Chu, Heteroepitaxial approach to explore charge dynamics across Au/BiVO$_4$ interface for photoactivity enhancement, Nano Energy 15 (2015) 625–633.

[39] W. Xiao, J.S. Chen, X.W. Lou, Synthesis of octahedral Mn$_3$O$_4$ crystals and their derived Mn$_3$O$_4$-MnO$_2$ heterostructures via oriented growth, CrystEngComm 13 (2011) 5685–5687.

[40] L. Zhu, Z. Chang, Y. Wang, B. Chen, Y. Zhu, W. Tang, Y. Wu, Core-shell MnO$_2$@Fe$_2$O$_3$ nanospindles as a positive electrode for aqueous supercapacitors, J. Mater. Chem. A 3 (2015) 22066–22072.

[41] Y.X. Zhao, Y. Zhang, H. Zhao, X.J. Li, Y.P. Li, L. Wen, Z.F. Yan, Z.Y. Huo, Epitaxial growth of hyperbranched Cu/Cu$_2$O/CuO core-shell nanowire heterostructures for lithium-ion batteries, Nano Res. 8 (2015) 2763–2776.

[42] K.A. Dick, S. Kodambaka, M.C. Reuter, K. Deppert, L. Samuelson, W. Seifert, L.R. Wallenberg, F.M. Ross, The morphology of axial and branched nanowire heterostructures, Nano Lett. 7 (2007) 1817–1822.

[43] L. Wang, M. Sakurai, H. Kameyama, Study of catalytic decomposition of formaldehyde on Pt/TiO$_2$ alumite catalyst at ambient temperature, J. Hazard. Mater. 167 (2009) 399–405.

[44] L. Wang, Q. Zhang, M. Sakurai, H. Kameyama, Development of a Pt/TiO$_2$ catalyst on an anodic alumite film for catalytic decomposition of formaldehyde at room temperature, Catal. Commun. 8 (2007) 2171–2175.

[45] Z. Wang, J. Pei, J. Zhang, Catalytic oxidization of indoor formaldehyde at room temperature – effect of operation conditions, Build. Environ. 65 (2013) 49–57.

[46] M. Ikegami, T. Matsumoto, Y. Kobayashi, Y. Jikihara, T. Nakayama, H. Ohashi, T. Honma, T. Takei, M. Haruta, Air purification by gold catalysts supported on PET nonwoven fabric, Appl. Catal. B-Environ. 134–135 (2013) 130–135.

[47] X. Wang, Y.D. Li, Synthesis and formation mechanism of manganese dioxide nanowires/nanorods, Chem. Eur. J. 9 (2003) 300–306.

[48] W. Xiao, H. Xia, J.Y.H. Fuh, L. Lu, Growth of single-crystal α-MnO$_2$ nanotubes prepared by a hydrothermal route and their electrochemical properties, J. Power Sources 193 (2009) 935–938.

[49] W. Xiao, D. Wang, X.W. Lou, Shape-controlled synthesis of MnO$_2$ nanostructures with enhanced electrocatalytic activity for oxygen reduction, J. Phys. Chem. C 114 (2009) 1694–1700.

[50] B.Y. Bai, J.H. Li, J.M. Hao, 1D-MnO$_2$, 2D-MnO$_2$ and 3D-MnO$_2$ for low-temperature oxidation of ethanol, Appl. Catal. B-Environ. 164 (2015) 241–250.

[51] F.Y. Cheng, T.R. Zhang, Y. Zhang, J. Du, X.P. Han, J. Chen, Enhancing electrocatalytic oxygen reduction on MnO$_2$ with vacancies, Angew. Chem.-Int. Ed. 52 (2013) 2474–2477.

[52] H. Huang, D.Y.C. Leung, Complete oxidation of formaldehyde at room temperature using TiO$_2$ supported metallic Pd nanoparticles, ACS Catal. 1 (2011) 348–354.